

Kinematics of the H α and H β broad line region in an SDSS sample of type 1 AGNs

N. Rakić,^{1,2}★

¹Physics Department, Faculty of Natural Sciences and Mathematics, University of Banjaluka, Mladena Stojanovića 2, 78000 Banjaluka, RS, Bosnia and Herzegovina

²Department of Astronomy, Faculty of Mathematics, University of Belgrade, Studentski trg 16, 11000 Belgrade, Serbia

Accepted XXX. Received YYY; in original form ZZZ

ABSTRACT

Here we investigate the kinematics of the part of the broad line region (BLR) in active galactic nuclei (AGNs) emitting H β and H α emission lines. We explore the widths and asymmetries of the broad H β and H α emission lines in a sample of high quality (i.e. high signal to noise ratio) spectra of type 1 AGN taken from the Data Release 16 of the Sloan Digital Sky Survey, in order to explore possible deviation from the gravitationally bound motion. To find only the broad component of H β and H α we use the FANTASY (Fully Automated pythoN Tool for AGN Spectra analYsis) code for the multi-component modeling of the AGN spectra and for careful extraction of the broad emission line parameters. We show that based on the broad line profiles widths and asymmetries, the BLR gas emitting H β and H α lines follows similar kinematics, and seems to be virialized in our sample of type 1 AGN.

Key words: line: profiles - galaxies: active - quasars: emission lines

1 INTRODUCTION

Determination of the mass of the supermassive black holes (SMBH) residing in the center of most if not all galaxies that have a bulge component, is an important factor for understanding the galaxy evolution and the interplay of the SMBH and its host galaxy (see e.g., a review [Kormendy & Ho 2013](#), and references therein). However, measuring the SMBH mass is still a complex task based on either resolving the region of the SMBH gravitational influence, for direct dynamical methods, or using various scaling relations for indirect mass estimates (see e.g., [Peterson 2014](#)). All of which are strongly dependant on the kinematics of the region which properties are being measured.

In case of galaxies hosting an active galactic nuclei (AGN), which could be traced to much higher redshift due their higher luminosity, the SMBH mass can be measured using broad emission lines, observed in so-called type 1 AGN (for a recent review see e.g., [Popović 2020](#)). One well-known method using the width of the broad emission-lines, assumes the that line-emitting gas (so-called broad-line region - BLR), surrounding the SMBH is virialized, i.e., the kinematics of the BLR gas is governed by the gravity of the SMBH (see e.g., [Peterson & Wandel 1999](#); [Sulentic et al. 2000](#); [Netzer 2015](#), etc.). However, there are indications that the BLR kinematics is more complex, due to possible presence of several emitting components (e.g., [Popović et al. 2004](#)), or radial motions, such as inflows or outflows (e.g., [Gaskell 2009](#); [Vietri et al. 2020](#)).

Usually, the virialization of the BLR is considered a priori and is widely used as an assumption when estimating the SMBH mass in AGNs from spectral parameters, i.e. the broad line width and the

BLR radius. Probing if the BLR gas kinematics is gravitationally bound to the SMBH, i.e. if the virialization holds and what would be the observational signatures to support this, is important for understanding when the BLR properties, namely the emission line widths, could be used to measure the SMBH mass (e.g., [Marziani & Sulentic 2012](#); [Jonić et al. 2016](#); [Popović et al. 2019](#)). This has great implications for the wide usage of scaling relations involving the emission line widths and fluxes to measure the SMBH mass from a single-epoch spectrum ([McLure & Jarvis 2002](#); [Dalla Bontà et al. 2020](#)). In case of low-luminosity near-by AGN, empirical correlations for the so-called virial mass based on the broad H α emission line are widely used ([Greene & Ho 2005](#); [Xiao et al. 2011](#)). For most AGNs, the width of H β line was mostly used as a virial broadening estimator of the SMBH mass ([McLure & Dunlop 2001](#); [Vestergaard & Peterson 2006](#)), e.g. it was used in the catalogue of Sloan Digital Sky Survey (SDSS) type 1 AGN ([Shen et al. 2011](#)). For more distant AGN, one should use UV lines, such as C IV ([Assef et al. 2011](#)) and Mg II ([Mejía-Restrepo et al. 2016](#)). Therefore, it is important to find different ways to test if the line-emitting gas is virialized.

[Popović et al. \(2019\)](#) investigated the kinematics of the H β and Mg II line emitting regions, and showed that the H β and Mg II core component seems to be virialized, concluding that Mg II could be used for the SMBH mass estimates if the Mg II core component is dominant. [Marziani et al. \(2022a\)](#) studied the virialization in UV lines, namely Al III λ 1860 doublet and the C III] λ 1909 line, and showed that they could be used as virial broadening estimators, similar to H β . Here we aim to investigate the kinematics of the H α and H β broad-line emitting-region by careful extracting the pure broad line profiles, and measuring the line widths and asymmetries. We aim to perform simultaneous multicomponent spectral fitting in order to

★ E-mail: nemanja.rakic@pmf.unibl.org

deblend the broad $H\alpha$ and $H\beta$ line from the satellite narrow lines and Fe II lines.

For this study, we use a sample of high quality (i.e. high signal to noise ratio) optical spectra collected for 946 low-redshift type 1 AGNs from the Sloan Digital Sky Survey (SDSS) Data Release 16 (Ahumada et al. 2020). We divide AGNs into two population A and B, based on a limit on the $H\beta$ line full width at half maximum (FWHM) ~ 4000 km/s, as around this width the clear change in the shape of the $H\beta$ line profile is seen (Sulentic et al. 2002). Population A and B objects are discussed to have significantly different physical properties (see e.g., Sulentic et al. 2000; Marziani et al. 2022b, and reference therein). These populations occupy different areas of the FWHM $H\beta$ - R_{FeII} space, which is known as the quasar main sequence primarily driven by Eddington ratio convolved with the line of sight orientation (Sulentic et al. 2000; Shen & Ho 2014; Marziani et al. 2022b). The parameter R_{FeII} is a measure of the optical Fe II emission, defined as the ratio of equivalent widths of Fe II emission in the range 4435–4685 Å and $H\beta$ broad line. In summary, Population B sources are showing broader emission line widths and weaker Fe II emission ($R_{\text{FeII}} \leq 0.5$), most likely having low Eddington ratio and being viewed at higher inclination angles. On the other hand, Population A sources are mostly associated with higher Eddington ratio, and show narrower broad emission lines and stronger Fe II emission ($R_{\text{FeII}} \geq 0.5$). These are believed to be viewed more face-on (see for a recent review Marziani et al. 2022b). We use the separation to population A and B object following the argument that the change in the line profile occurs after 4000 km s^{-1} (Marziani et al. 2018), as well as to have equally populated sub-samples.

The paper is organized as follows: section 2 describes the data sample and the performed analysis, section 3 gives the theoretical justification of our approach, section 3 presents and discuss the obtained results, and finally, section 4 outlines the conclusions. For calculating the luminosity through the luminosity distance, we used the cosmological parameters $H_0 = 70 \text{ km s}^{-1} \text{ Mpc}^{-1}$, $\Omega_m = 0.30$, and $\Omega_\Lambda = 0.70$.

2 DATA & METHODS

2.1 Sample of type 1 AGNs

In order to retrieve a large sample of type 1 AGN having high-quality spectra, i.e. with high signal-to-noise (S/N) ratio, we explored the SDSS Data Release 16 (DR16, Ahumada et al. 2020). DR16 is the fourth data release of the fourth phase of the survey (SDSS-IV), including the complete data set of optical single-fibre spectroscopy of the SDSS through February 2019 (see Smees et al. 2013, for details on SDSS spectrographs and spectral resolution). These data represent the culmination of SDSS 20 year mission in collecting optical spectra to map the 3D structure of the Universe¹. We used Structured Query Language (SQL) to query the SDSS DR16 SkyServer search tools² data table ‘specobjALL’, choosing spectra that follow these three simple criteria:

(i) redshift $z < 0.4$ with $z_{\text{warning}} = 0$ to ensure that both $H\beta$ and $H\alpha$ are included, i.e. spectra cover the wavelength region at least up to 7000 Å ;

(ii) signal to noise ratio in g-band higher than 30, to ensure high-quality spectra around $H\beta$ emission lines;

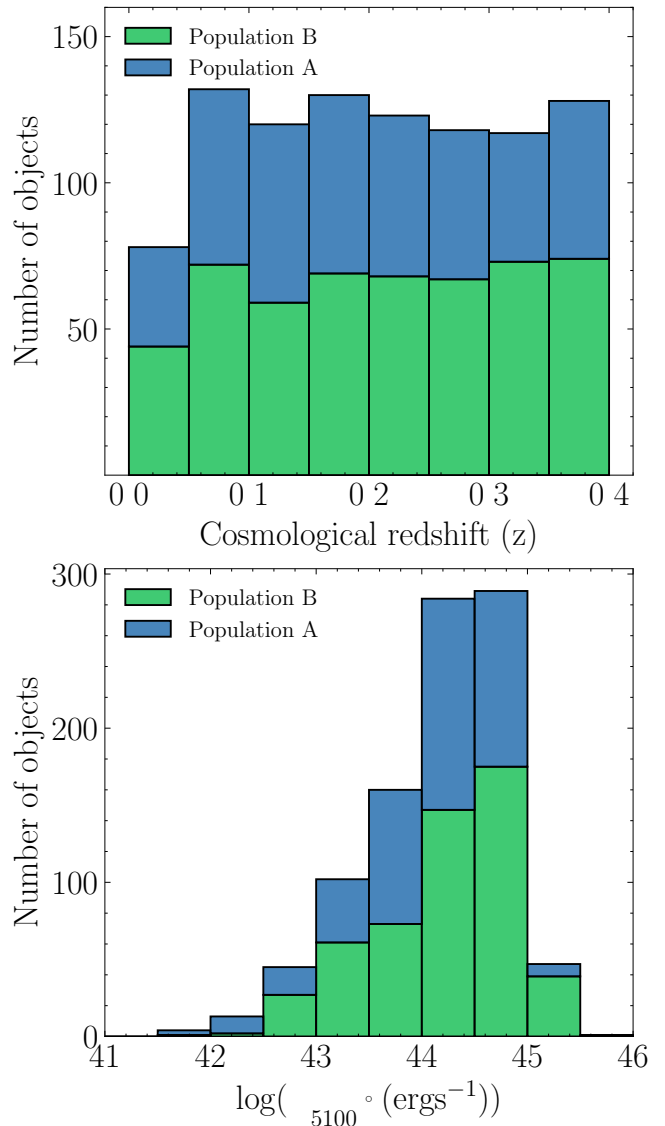


Figure 1. Histograms of the cosmological redshift (upper) and continuum luminosity at 5100 Å (bottom) showed as stacked bars of population A (blue) and population B (green) objects.

(iii) objects classified as "QSO".

The SQL query returned 960 objects. After visual inspection of preliminary spectral fittings (see Section 2.3), we excluded 14 objects with poor fitting results, typically due to bad pixels near emission lines of interest, or strong cosmic ray presence. This left 946 objects in the sample which was further studied in more details. Further in the analysis, we divide the total sample into two sub-samples based on the broad $H\beta$ FWHM to: i) population B with $\text{FWHM}(H\beta) > 4000$ km/s, resulting with 526 objects, and ii) population A with $\text{FWHM}(H\beta) < 4000$ km/s giving 420 objects. Furthermore, we discuss as a subset of population A object, so-called extreme population A, with strong iron emission and $R_{\text{FeII}} > 1$ (Marziani et al. 2022b), which consist of 82 objects.

¹ www.sdss.org/dr16/spectro/

² www.skyserver.sdss.org/dr16/en/tools/search/sql.aspx

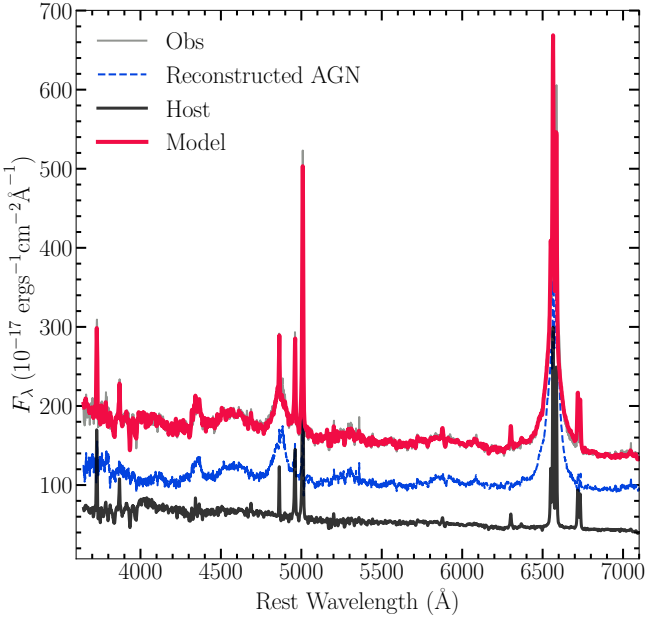


Figure 2. Example of the PCA host reconstruction using in case of the object SDSS J101912.56+635802.6. Observed flux is denoted with gray color, the reconstructed model with red, host galaxy flux is given with green, and pure reconstructed AGN (observed flux - host galaxy flux) with blue.

2.2 Properties of the selected sample

We briefly discuss the properties of our sample of 946 type 1 AGN. Fig. 1 give histograms of the cosmological redshift z (upper panel) and continuum luminosity $L_{5100\text{\AA}}$ (lower panel) for the total sample, shown as stacked bars of population A (blue) and population B (green) objects. Our total sample is uniformly sampled across the selected range of redshift, as well as both subsets. Most of the objects in the total sample (95%) have the continuum luminosity $\log(L_{5100\text{\AA}} \text{ erg s}^{-1})$ in the range [42.65-45.11]. The distribution is having the median $\log L_{5100\text{\AA}} = 44.30$ and is asymmetric toward higher-luminosity AGN, as is expected for the sample of SDSS type 1 AGNs (see Liu et al. 2019, and their Figure 9).

We tested if different selection of S/N ratio influence the sample properties. Putting less strict limit for $S/N > 20$, the redshift distribution remains the same, and there is no significant influence on the distribution of luminosities, whereas the sample size increase roughly 3 times. However, since the main aim of this work is to carefully extract the broad $H\alpha$ and $H\beta$ emission lines and measure their properties, lowering the limit to S/N will increase the presence of noisy spectra, which will increase the scatter of measured emission line-parameters.

Therefore, the final selected sample consists of the AGNs with high-quality spectra, in which we can analyse the emission-line shapes very precisely.

2.3 Spectral fittings and analysis

For the AGN spectral analysis, we used python-based code for multi-component spectral fitting - FANTASY (Fully Automated python Tool for AGN Spectra analysis)³, first used in Ilić et al. (2020).

³ This is an open-source code, soon to be available on GitHub

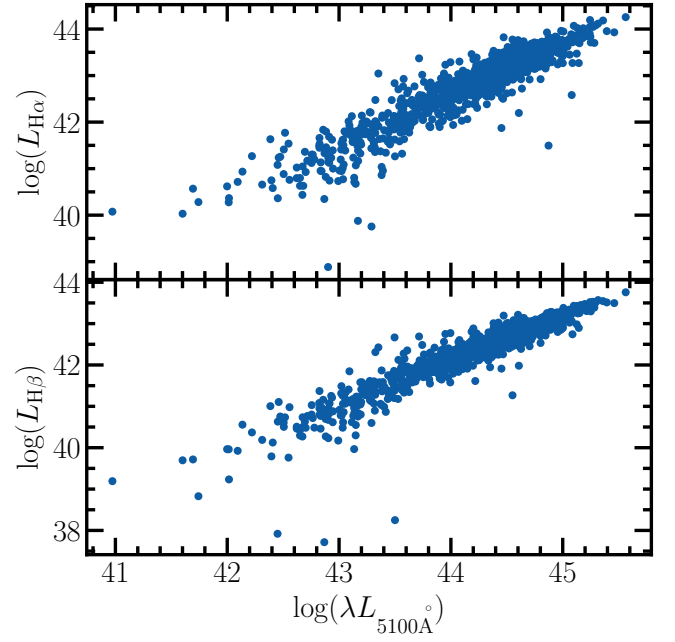


Figure 3. Luminosity of the extracted broad $H\alpha$ (upper panel) and $H\beta$ (bottom panel) line vs. AGN continuum luminosity $L_{5100\text{\AA}}$, in erg/s.

The first step is the preparation of spectra for the fittings. We corrected the spectra for Galactic extinction using dust map data from Schlegel et al. (1998), as well as for the cosmological redshift using the redshift provided in the SDSS database. Intending to get pure AGN spectra, we firstly have removed host galaxy contamination by applying the PCA method explained in Vanden Berk et al. (2006). According to Vanden Berk et al. (2006) majority of spectra can be reconstructed using the linear combination of 10 QSO eigenspectra from Yip et al. (2004b) and 5 galaxy eigenspectra from Yip et al. (2004a). We remove host galaxy contribution by subtracting the reconstructed host galaxy from the observed spectrum. Example of host reconstruction is given in the Fig. 2.

Further, we applied simultaneous multi-component spectral fitting to remove narrow and satellite lines to extract the broad component of both $H\beta$ and $H\alpha$ lines⁴. We fitted all spectra in the rest wavelength range $\sim 4200\text{--}7000 \text{\AA}$ using the same model. The used model consisted from:

- (i) broken power law continuum;
- (ii) hydrogen $H\alpha$, $H\beta$ and $H\gamma$ lines with three Gaussian components (two broad and one narrow);
- (iii) helium lines He I 4471 \AA , He I 5877 \AA , and He II 4686 \AA ;
- (iv) narrow emission lines, all fixed to have the same shifts and widths as [O III] 5007 \AA : [O III] 4363 \AA , [O III] 4959, 5007 \AA , [N II] 6548, 6583 \AA , [S II] 6716, 6731 \AA ; the ratio of [O III] 4959,5007 \AA and [N II] 6548,6583 \AA doublets were fixed to 3 (Dimitrijević et al. 2007; Dojčinović et al. 2022); the list of used narrow lines contains also nebular line [O I] 6300 \AA and [O I] 6364 \AA , but these were seldom identified;
- (v) the broad component of the [O III] doublet (Kovačević-Dojčinović et al. 2022),

⁴ Spectral fittings were performed using the SUPERAST computer cluster of the University of Belgrade - Faculty of Mathematics, Department of Astronomy (Kovacevic et al. 2022).

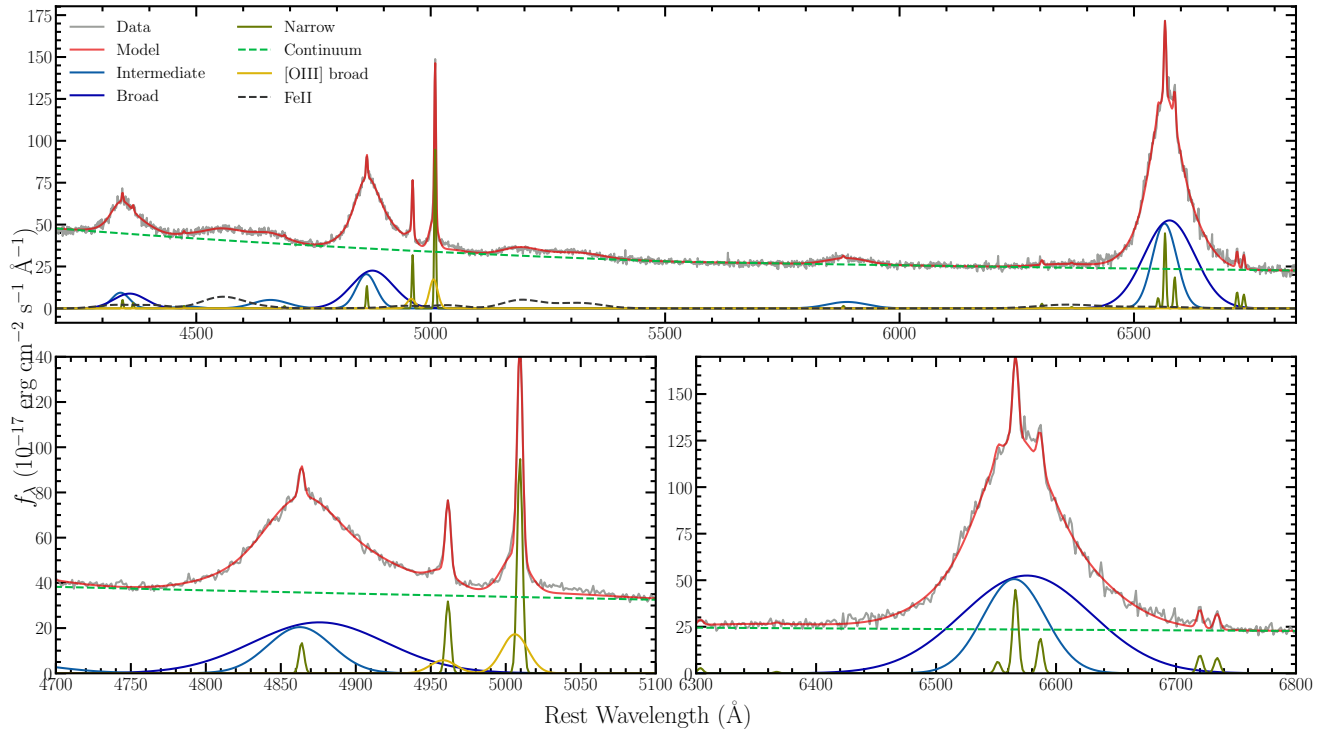


Figure 4. Multi-component simultaneous fitting of the $\lambda\lambda 4200\text{--}7000\text{ \AA}$ wavelength region for the object SDSS J074910.59+284214.5, which is an example of Population B object. Below the observed (gray) and modeled (red) spectrum, the broken power-law continuum (green dashed) and all Gaussian components are shown (blue, dark-blue - broad components of $H\alpha$ and $H\beta$; green - narrow lines; yellow - [O III] broad component). Black dashed line indicate the Fe II model. Below two panels show the zoom-in of the $H\beta$ and $H\alpha$ line region.

(vi) optical Fe II model based on the atomic data of the transitions (see for details Kovačević et al. 2010; Shapovalova et al. 2012; Kovačević-Dojčinović & Popović 2015).

The total sample was fitted automatically with this model. We have visually inspected all the results of the fittings. To illustrate the performance of the automated spectral fittings, we plot in Figure 3, how the luminosity of the extracted broad line $H\alpha$ and $H\beta$ fluxes behaves with the continuum luminosity $L_{5100\text{ \AA}}$. As expected by the photoionization theory explaining the origin of the broad emission lines (Osterbrock & Ferland 2006; Netzer 2013), as well as shown by observations (e.g., Ilić et al. 2017; Dalla Bontà et al. 2020), the broad emission line fluxes are strongly correlated with the AGN continuum flux. This supports that the fitting results are reasonable. Examples of the fits for a population B object is given in Fig. 4, and for Population A in Fig. 5. The goodness of the best fitting results were evaluated using the χ^2 parameter.

Once the broad $H\alpha$ and $H\beta$ line profiles have been extracted, we measured their following properties (Figure 6). The full width at different level of maximum intensity are: i) full width half maximum - FWHM, ii) full width quarter maximum - FWQM, and iii) full width at 10% maximum - FW10M. The asymmetry of the line, which are indicator of the intrinsic gravitational redshift (see Section 3 for details), is measured as a difference between the centroid of the line at different levels of intensity and position of the peak of the broad line. Thus we have also measured corresponding three asymmetries at 50%, 25%, and 10% of the maximum intensity, denoted as z_{50} , z_{25} , z_{10} , respectively (Figure 6). We also measured the emission line dispersion σ calculated as the second moment of the broad line profile using Peterson et al. (2004) formalism (see their Equations 4 and 5). Line widths and asymmetries were measured from the modeled

broad line profiles, whereas the line dispersion was measured from the clean broad line profile, which is obtained from the observed spectra from which the contribution of the underlying continuum and satellite lines has been subtracted. The uncertainties are estimated as 1σ errors derived from random subsets of N spectra (as in e.g., Kollatschny & Zetzl 2011).

In addition, we measured the broad line fluxes, as well as the Fe II optical emission in the range $4435\text{--}4685\text{ \AA}$ to get the R_{FeII} parameter. The AGN continuum flux at 5100 \AA was measured as a median of the integral in $5080\text{--}5120\text{ \AA}$ range from the reconstructed pure AGN spectra (Figure 2). The luminosity was calculated using the luminosity distance obtained from the redshift and adopted cosmology (see Section 1).

Table 1 lists the all measured spectral parameters, that is: the object ID, redshift, continuum luminosity $L_{5100\text{ \AA}}$, optical Fe II emission R_{FeII} , full width and asymmetries at different level of maximum intensity for $H\alpha$ and $H\beta$ broad line. The full table is available online as supporting information.

3 KINEMATICS AND THE VIRIALIZATION ASSUMPTION OF THE BLR

To investigate if the kinematics of the broad-line emitting gas is primarily driven with the SMBH gravitational force, that is to study the virialization of the BLR, we start from the following arguments:

- (i) the ratio of the full line widths at different levels of line intensities should be constant across the luminosity scale;
- (ii) the gravitational redshift, here considered as an intrinsic shift,

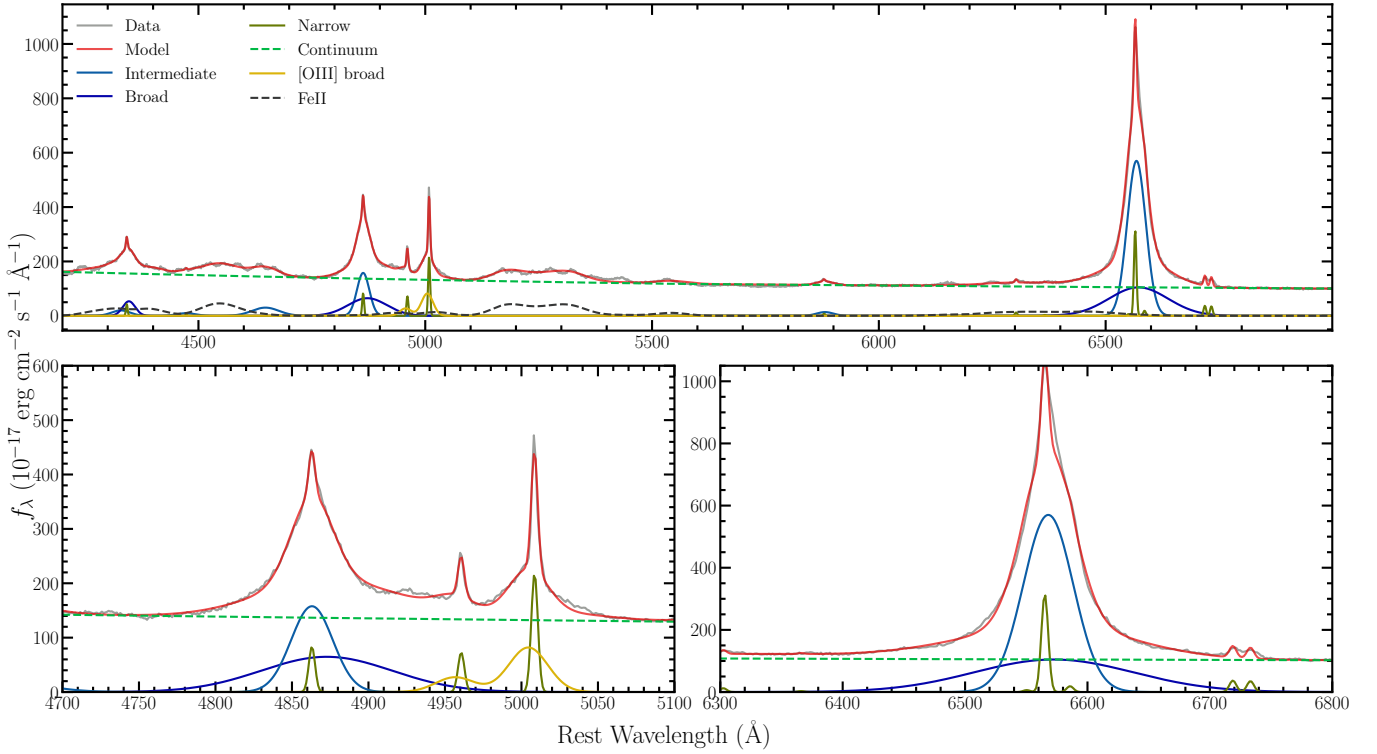


Figure 5. The same as in Figure 4 but for the object SDSS J135550.20+204614.5, which is an example of the Population A object.

Table 1. Measured spectral parameters for the sample of 946 SDSS type 1 AGN. Columns are: SDSS object ID, redshift, continuum luminosity $\log \lambda L_{5100\text{\AA}}$, optical Fe II emission R_{FeII} , full width at half (FWHM), quarter (FWQM), and 10% (FW10M) of maximum intensity, and corresponding asymmetries (z_{50} , z_{25} , z_{10}). Line widths and asymmetries are listed for both H α and H β broad line. The full table is available online as supporting information.

SDSS ID	z	$\lambda L_{5100\text{\AA}}$ [erg s $^{-1}$]	R_{FeII}	FWHM [kms $^{-1}$]		FWQM [kms $^{-1}$]		FW10M [kms $^{-1}$]		z_{50} [kms $^{-1}$]		z_{25} [kms $^{-1}$]		z_{10} [kms $^{-1}$]	
				H β	H α	H β	H α	H β	H α	H β	H α	H β	H α	H β	H α
SDSS J145824.46+363119.5	0.25	44.51	0.68	2120	2100	3800	3200	6860	5940	0	0	150	0	150	0
SDSS J095302.64+380145.2	0.27	44.55	0.25	3210	3020	5550	4620	8320	7220	290	0	1020	140	1460	730
SDSS J004222.18-055823.4	0.2	44.02	0.43	3650	2700	5250	4300	6860	6210	0	0	-180	0	-270	
SDSS J142245.78+630739.1	0.16	43.94	0.59	3070	2240	5110	3570	7450	5530	290	0	730	90	1020	230
SDSS J103208.42+405508.8	0.4	44.89	0.56	4160	3890	7080	6030	10370	9140	360	0	1240	180	1750	370
SDSS J225603.37+273209.5	0.36	45.25	0.22	5460	4540	7800	7530	9980	10560	0	2520	0	3210	0	3210
SDSS J032559.97+000800.7	0.36	44.8	0.11	6920	6850	9830	9820	12670	12650	0	460	0	500	0	500
SDSS J140839.00+630600.5	0.26	44.51	0.18	5250	5120	7810	7500	10650	10290	0	180	0	460	0	870
SDSS J224113.54-012108.8	0.06	43.21	0.09	6740	5760	9740	8140	12600	10560	2640	-90	2710	-90	2780	-140
SDSS J105007.75+113228.6	0.13	44.51	0.34	2190	2330	3650	3560	6780	5850	0	0	290	0	950	370

should be related to the square of the full line widths at different levels of line intensities.

These arguments are derived from the following. Popović et al. (2019) discussed that different region of the gas clouds from the BLR are contributing to the different part of the emission line (see also Sulentic et al. 2000, for a review). Thus, emission of the regions closer to the SMBH will contribute to the line wings, whereas further regions will dominate the core of the emission line. Emission line widths can be used as a measure of the gas velocity. One can assume that widths at various scale of the line intensity, actually represent velocity of the different regions in the gas cloud, i.e. broader widths at lower levels of line intensities are indicators of the gas clouds closer to the SMBH.

According to the virial theory we have (see e.g. recent review by

Popović 2020, and reference therein):

$$M_{\text{BH}} = f_{\text{line}} \frac{\text{FWHM}^2 R_{\text{line}}}{G}, \quad (1)$$

where M_{BH} is mass of the black hole, f_{line} is the virial factor accounting for the inclination and geometry of the BLR, R_{line} is the distance to the line-emitting region, and G is gravitational constant. Using Eq. 1, we can write that:

$$M_{\text{BH}} = f_{\text{line}} \frac{\text{FWHM}^2 R_{\text{line},1/2}}{G}, \quad (2)$$

$$M_{\text{BH}} = f_{\text{line}} \frac{\text{FWXM}^2 R_{\text{line},X}}{G}, \quad (3)$$

where $R_{\text{line},1/2}$ is the distance to the line-emitting gas with observed

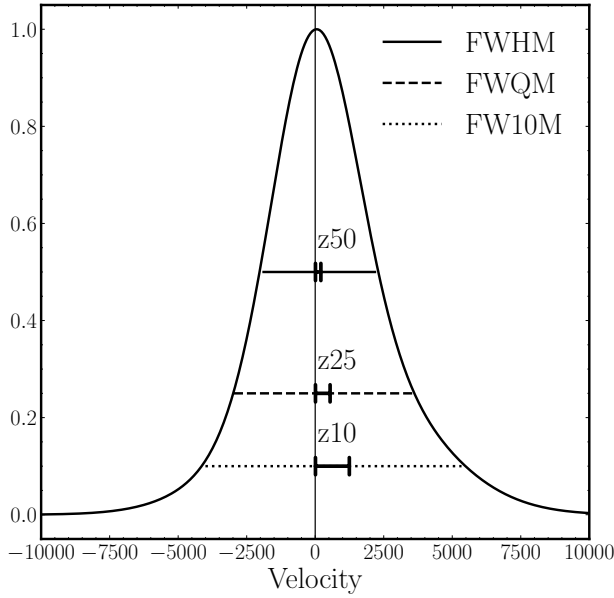


Figure 6. Normalized broad line profile with indicated measured parameters: full widths at different level of maximum intensity - at 50% FWHM, at 25% FWQM, and at 10% FW10M. The corresponding red asymmetries were also indicated with z_{50} , z_{25} , z_{10} .

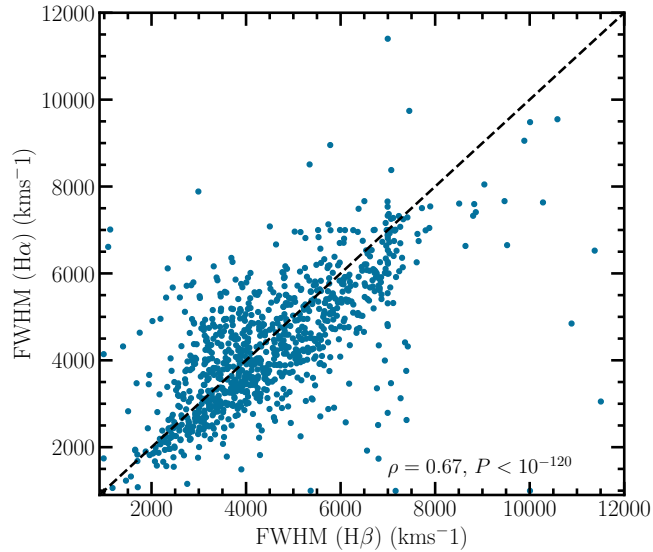


Figure 7. FWHM of $H\beta$ vs. FWHM of $H\alpha$ broad line for the total sample of type 1 AGNs. The one-to-one ratio is shown as dashed line. Pearson correlation coefficient together with corresponding P-value is also given.

velocities measured with FWHM, whereas $R_{\text{line},X}$ is distance from the SMBH to the gaseous clouds with observed velocity indicated by the full width at some arbitrary X percentage of the line maximum intensity (FWXM). If we assume that the f -factor for the emission-line profiles measured at the half and X percentage of the maximum intensity are the same, combining Eqs. 2 and 3 we can write that:

$$\frac{\text{FWXM}^2}{\text{FWHM}^2} = \frac{R_{\text{line},1/2}}{R_{\text{line},X}}. \quad (4)$$

In addition, several reverberation mapping studies discovered an empirical relationship between the distance to the line-emitting region

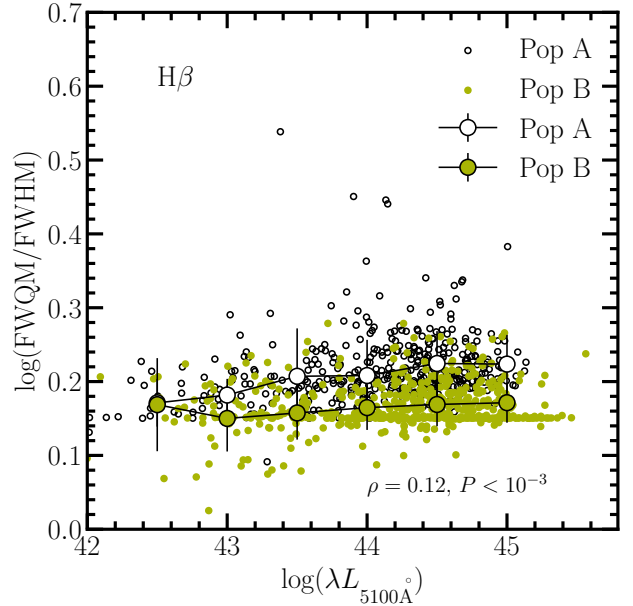
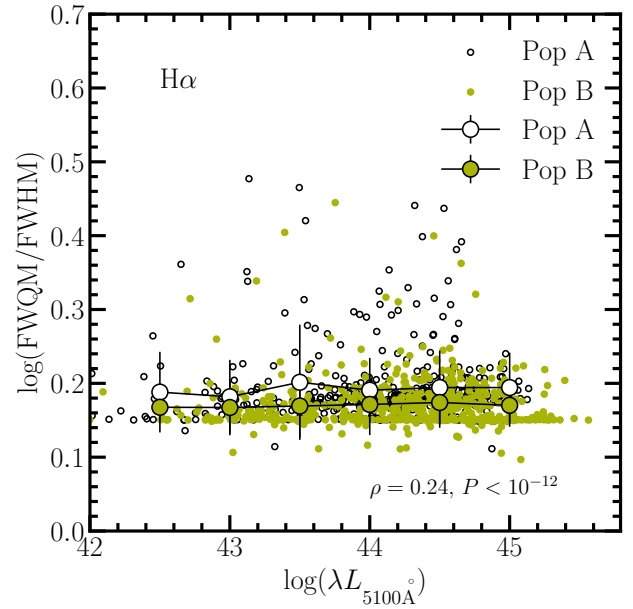


Figure 8. Ratio of the FWHM to FWQM vs. $\log(L_{5100\text{\AA}})$ for $H\alpha$ (upper panel) and $H\beta$ (bottom panel) for the population A (open circles) and population B (green circles) sub-samples. The average values for aggregated continuum luminosity bins (0.5 dex) are also given (larger circles with errorbar). Pearson correlation coefficient ρ together with corresponding P-value is denoted on each plot.

R_{BLR} and central continuum luminosity L_{cnt} (see: Kaspi et al. 2000; Bentz et al. 2006), which can be written in a form:

$$\log R_{\text{BLR}} = a \cdot \log L_{\text{cnt}} + b. \quad (5)$$

This relation should hold for the distance to different line-emitting regions. Thus, taking into the account Eqs. 4 and 5 one can expect that the logarithm of ratio of full widths at various intensity levels of the emission line should be independent from the continuum luminosity. We will explore this assumption within our analysis to test if the virialization holds for the $H\alpha$ and $H\beta$ line-emitting regions.

Zheng & Sulentic (1990) argued that asymmetry of the $H\beta$ line wings can be explained with the gravitational redshift (see also e.g.,

Netzer 1977; Corbin 1995; Kollatschny 2003, etc.). The red asymmetry has been discussed in terms of gravitational redshift in other lines as well, such as the UV Fe III lines (Mediavilla et al. 2018). Punsly et al. (2020) also report the strong red asymmetry in UV Mg II and C IV lines of a sample of blazars, which was discussed in terms of gravitational origin.

For the emitting gas at a distance R from the SMBH, where M_{BH} is the mass of the black hole, in the weak field approximation the combined gravitational and transverse Doppler redshift will tend to (see e.g., Bon et al. 2015; Liu et al. 2017; Mediavilla et al. 2018; Popović et al. 2019; Liu et al. 2022):

$$z_G = \frac{3}{2} \frac{GM_{\text{BH}}}{c^2 R} \quad (6)$$

where c is speed of the light. Note that the transverse Doppler redshift being inversely proportional to the Lorentz factor, is entirely a special relativistic effect but, being independent from orientation, cannot be distinguished from the gravitational contribution. Previous analysis of AGN spectra suggested that the broad line redshifts could be mainly the result of gravitational redshift (see e.g. discussion in Mediavilla et al. 2018, and references therein).

If one assume that the radius R , in Eqs. (1) and (6), represent the same photometric radius, it is expected to have:

$$z_G \sim \text{FWHM}^2. \quad (7)$$

The asymmetry of the line, thus the gravitational redshift, can be quantified as a difference between the centroid of the line at different levels of intensity and position of the peak of the broad line (for more explanation see: Jonić et al. 2016). Accordingly, if the broad-line emitting gas is virialized, one can expect to have linear relationship between logarithms of z_G and FWHM of the line (see also Popović et al. 2019). We use also this to explore the virialization in the BLR.

We test the kinematics of the BLR emitting $H\alpha$ and $H\beta$ emission lines by exploring relation between ratio of FWHM/σ vs. FWHM. Especially, because the line dispersion σ is generally more sensitive to the line wings and less to the line core (Collin et al. 2006; Kollatschny & Zetzl 2011). The ratio of FWHM/σ depends on the line profile: for gaussian profile we have $\text{FWHM}/\sigma = 2.35$, for rectangular function ratio is 3.46, while for Lorentzian profiles $\text{FWHM}/\sigma \rightarrow 0$ (see e.g Kollatschny & Zetzl 2013). According to Collin et al. (2006) and also Kollatschny & Zetzl (2011) broad lines have tendency to have flat-topped profiles, whereas narrower lines have more extended wings. Collin et al. (2006) divided their sample of AGN into two populations based on the line profile: $\text{FWHM}/\sigma_{\text{line}} < 2.35$ (population 1) and $\text{FWHM}/\sigma_{\text{line}} > 2.35$ (population 2), finding that these basically correspond to separation to population A and B suggested by Sulentic et al. (2000). Instead, Kollatschny & Zetzl (2011, 2013) showed that there is more a continuous transition from narrow to broad-line objects. We explore these findings in our sample.

4 RESULTS & DISCUSSION

For the sample of 946 SDSS type 1 AGNs, we analyze in more details the measured $H\alpha$ and $H\beta$ broad line parameters, i.e., full widths and asymmetries at different levels of maximum intensities.

In Figure 7 the FWHM of $H\beta$ vs. FWHM of $H\alpha$ broad line is plotted, together with the one-to-one line to guide the eye. It is clear that the $H\alpha$ and $H\beta$ line widths are similar and well correlated (Pearson correlation coefficient $\rho = 0.67$), supporting that similar kinematics of their emitting regions.

In order to test whether arguments from Section 3 are fulfilled,

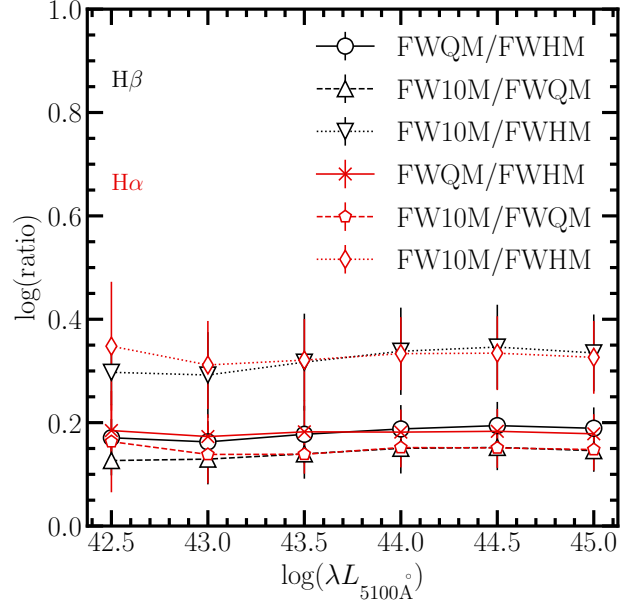


Figure 9. Logarithms of different line width ratios (denoted in upper right corner) across the luminosity scale. The values are averaged within continuum luminosity bins of 0.5 dex.

we explored relation between line widths and luminosity, as well as line widths and asymmetries. We start with the logarithm of the ratio of the full widths at quarter (FWQM) and half (FWHM) maximum intensity of both broad $H\beta$ and $H\alpha$ lines with the continuum luminosity at 5100\AA (Fig. 8). Furthermore, we aggregate data into continuum luminosity bins (0.5 dex), starting with $\log(\lambda L_{5100\text{\AA}})$, and give their average values. We separately considered Population A and B sub-type of AGNs. From Fig. 8 it is straightforward to realise that widths ratio is rather constant across the luminosity scale for both $H\alpha$ and $H\beta$ line. This is supported with the very low level of correlation (Pearson correlation coefficients are 0.24 and 0.12 for $H\alpha$ and $H\beta$, respectively). The constant trend is even more emphasized if we take the data aggregated in luminosity bins. The deviation of the trend is noticeable in the lower continuum bins, that is probably due to small number of data used for aggregation. We tested this for the ratios of all other measured line widths (FWHM, FWQM, FW10) and presented in Figure 9. The findings are the same, there is no trend seen in the ratios of line widths across different luminosities.

Popović et al. (2019) argued that contribution to different parts of the broad line are coming from different locations withing gaseous clouds surrounding the SMBH. Wings of the line are originating in clouds closer to the SMBH, whereas the line core is form the outer parts. If gas is virialized it is natural to assume that relation given in Eq. 7 is held across all the regions contribution to the emission line. With all above, if the gas is virialized we expect that logarithm of ratios of full widths should be constant across different continuum luminosity. One can see from the Fig. 8 that our findings are in line with the virial theory, and the kinematics of $H\alpha$ and $H\beta$ broad-line emitting-region is driven by the SMBH. Furthermore, clearly there is no much difference if one separately observe Population A and B types of AGNs.

Further, we observe whether the second arguments, involving the gravitational intrinsic redshift (Section 3) is applicable for our sample. Following Eq.7, in Figure 10 we plot correlations between the red asymmetry (i.e., gravitational redshift) measured at 50 (top panels), 25 (middle panels), and 10 (bottom panels) percent of line intensity

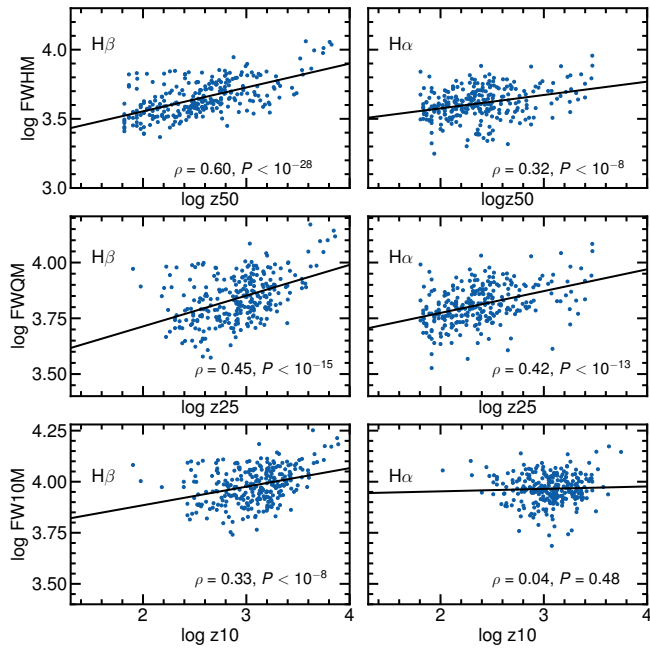


Figure 10. Correlation between asymmetry (i.e. gravitational redshift) measured at 50 (top panel), 25 (middle panels), and 10 (bottom panels) percent of line intensity versus corresponding full widths of the broad $H\beta$ (left), and $H\alpha$ line (right). Best linear fitting is given as a solid line. Pearson correlation coefficient, together with P-value is denoted on each plot.

versus corresponding full widths of the broad $H\beta$ (left) and $H\alpha$ line (right). We exclude from the analysis, detected asymmetries below the SDSS instrumental resolution of 70 km s^{-1} . Figure 10 reveals that the line widths at half and quarter maximum intensity are well-correlated with the corresponding asymmetries, being a measure of the intrinsic gravitational redshift. The correlations are particularly solid in case of FWHM of $H\beta$ and $H\alpha$, which is supported with the Pearson correlation coefficient of 0.60 and 0.45, respectively (denoted on each plot in Figure 10). The asymmetry measured in line wings is stronger, and show weaker correlation with the corresponding width (see FW10M vs. z_{10} in Figure 10, bottom plots), being practically absent in case of $H\alpha$ line. These are indicating that possibly the region contributing to the line-wings, especially in $H\alpha$, is not virialized, i.e., there are possible presence of radial motions such as inflows/outflows (Popović et al. 2019). We note that measurements in the line wings are most sensitive to the estimates of the underlying continuum, which is simultaneously fitted during this automated fitting procedure.

The mean and root-mean-square (rms) profiles of the normalized $H\alpha$ and $H\beta$ broad line are shown in Figure 11. Both mean profiles for the total sample (Figure 11, upper panel) are symmetric, and practically identical. The lack of asymmetry in $H\beta$ line was already noted by Popović et al. (2019) for $H\beta$ line. These authors also showed that in case of Mg II and $H\beta$ line, the largest difference is seen in the line wings. However, here we see no difference in the mean profiles of $H\alpha$ and $H\beta$ (Figure 11, upper panel). We tested also is there any difference between the mean and rms profiles in population A and B (Figure 11, middle and bottom panels). As expected, population B mean profile is wider, but both are symmetric, with very subtle red asymmetry seen in $H\alpha$ line.

All these results support that the BLR emitting Hydrogen Balmer

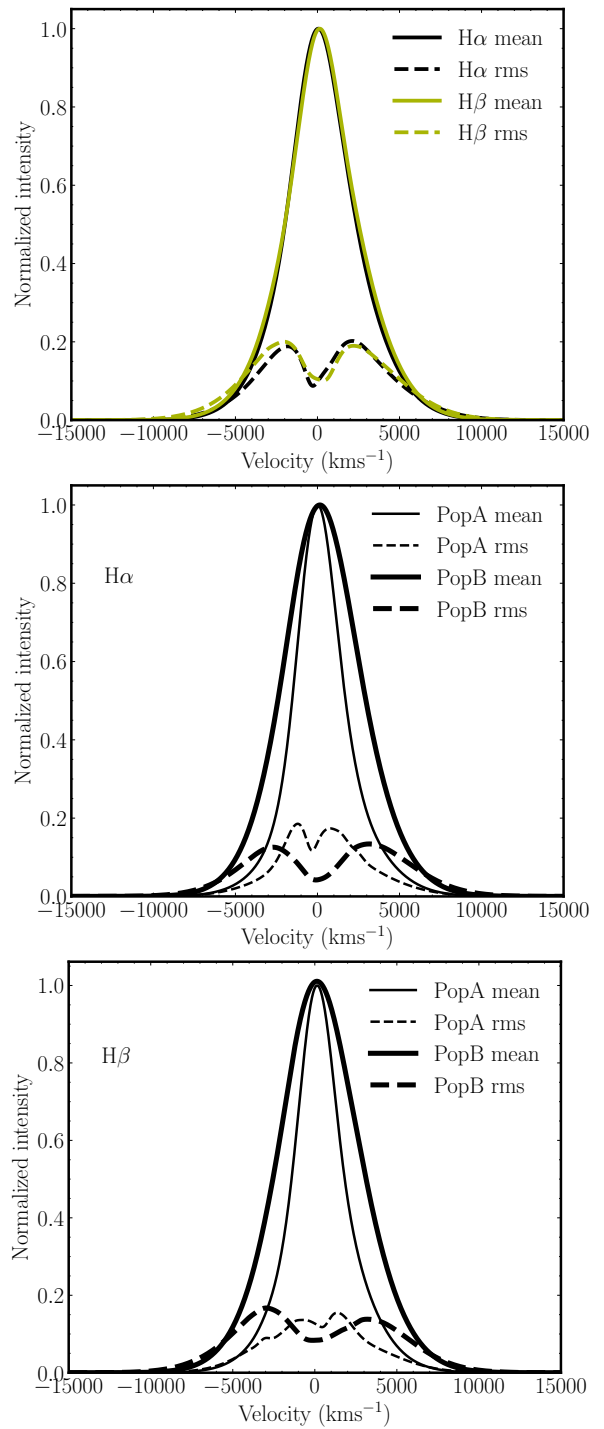


Figure 11. Upper: mean (full line) and rms (dashed line) of broad lines $H\alpha$ (black) and $H\beta$ (green) of the total sample. Middle: mean (full line) and rms (dashed line) of broad $H\alpha$ for the Population A (thin black line) and Population B (thick black line). Bottom: same as in the middle, but for the broad $H\beta$ line.

lines is virialized, i.e., the gas motion is primarily driven by the SMBH gravity.

We tested how the asymmetry, measured in the $H\beta$ line at the 50% of line maximum, differs across the AGN main sequence (Figure 12). First we note that our sample covers nicely the known main-sequence elbow shape in the $\text{FWHM}(H\beta) - R_{\text{FeII}}$ plane (Sulentic

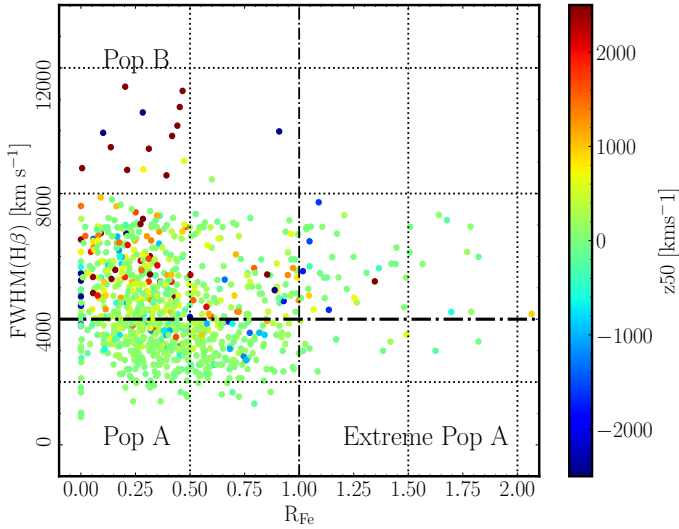


Figure 12. Location of the studied sample in the $\text{FWHM}(\text{H}\beta) - R_{\text{FeII}}$ plane (so-called AGN main sequence) showing red and blue asymmetry in the $\text{H}\beta$ line. Dot-dashed horizontal ($\text{FWHM}(\text{H}\beta)=4000$ km/s) and vertical ($R_{\text{FeII}}=1$) line divide the Population B, Population A, and extreme population A. The colorbar indicates the asymmetry measured at half maximum $z50$ in km/s.

et al. 2000; Marziani et al. 2001; Shen & Ho 2014). In case of population A, on average, asymmetry does not depend on the position of the object in the $\text{FWHM}(\text{H}\beta) - R_{\text{FeII}}$ plane. However, population B object show presence of more asymmetric profiles (see colorbar in Figure 12). Zamfir et al. (2010) showed that the population B object with broader profiles show higher red asymmetry. We present in Figure 13 histogram of the asymmetries measured at 50%, 25%, and 10% percent of line intensity for the broad $\text{H}\alpha$ and $\text{H}\beta$ line for both Population A and Population B objects. The majority of object show no (or very weak) asymmetry as measured with $z50$ (left panels, Figure 13), with population B object showing more asymmetric profiles in $\text{H}\beta$ line (as also concluded from Figure 12). When measuring the asymmetry in line wings (see middle and left panels, Figure 13), the number of object showing red asymmetry increases, especially in $\text{H}\beta$ line. However, this could be due to fitting poorly accounting for the Fe II contribution, as well as estimates of the underlying continuum, for which the line wings are the most sensitive. On the other hand, this could be also due to the presence of radial motion, as already discussed.

In the Figure 14 we presented the ratio of FWHM/σ vs. FWHM for the $\text{H}\alpha$ (open circles) and $\text{H}\beta$ (green circles) broad lines. The results show that the broad line profiles vary systematically with the increase of the line widths in the same manner for both $\text{H}\alpha$ and $\text{H}\beta$. Profiles of broader lines tend to be more flat-topped, whereas the narrower profiles have more prominent line wings (Collin et al. 2006; Kollatschny & Zetzl 2011). These findings are supporting the general trend found by Kollatschny & Zetzl (2011), that the line-broadening is dominantly by rotation. We also see the same smooth transition between population A and B, both in $\text{H}\alpha$ and $\text{H}\beta$, supporting our previous discussion that they follow the same kinematics.

5 CONCLUSIONS

In this work we study the kinematics of the BLR in a sample of 946 type 1 AGN selected from the SDSS DR16 only to have high S/N ratio and contain both $\text{H}\alpha$ and $\text{H}\beta$ emission lines. We perform careful extraction of the broad $\text{H}\beta$ and $\text{H}\alpha$ line from the pure AGN spectra, and measure their width and asymmetry. Our conclusions can be summarized as:

- (i) the FWHM of $\text{H}\alpha$ and $\text{H}\beta$ are well correlated, indicating that the kinematics of the regions emitting these lines is the same. This is supported with symmetric mean $\text{H}\alpha$ and $\text{H}\beta$ broad line profiles, being almost identical;
- (ii) the ratio of the full widths at quarter and half maximum intensity of $\text{H}\alpha$ and $\text{H}\beta$ lines are remaining the same across the luminosity scale. This applies also for all combinations of other line widths;
- (iii) the line red asymmetries, measured at different levels of line intensities, as tracers of the intrinsic gravitational redshift, correlates well with the corresponding line widths. The stronger correlation is seen in $\text{H}\alpha$ and $\text{H}\beta$ line widths at half and quarter maximum, whereas there is weaker or no correlation in the line-wings, indicating possible contribution of radial motions, such as inflows/outflow, to the line wing;
- (iv) our findings supports that the $\text{H}\alpha$ and $\text{H}\beta$ line emitting regions are having similar virialized kinematics, i.e. the gas motion is primarily driven by the gravitational force of the supermassive black hole. However, at highest velocities of the gas, which is reflecting in the line wings, there could be some signature of radial motions.

ACKNOWLEDGEMENTS

Author would like to thank the anonymous referee whose comments and suggestions helped to improve and clarify this manuscript, and to Dragana Ilić and Luka Č. Popović for many discussions throughout the work on this paper, as well as for careful reading of the manuscript and suggestions for improvements. Spectral fittings presented in this publication were performed using the SUPERAST computer cluster of the University of Belgrade - Faculty of Mathematics, Department of Astronomy (<http://astro.math.rs>).

This publication makes use of public SDSS data. Funding for the Sloan Digital Sky Survey IV has been provided by the Alfred P. Sloan Foundation, the U.S. Department of Energy Office of Science, and the Participating Institutions. SDSS-IV acknowledges support and resources from the Center for High Performance Computing at the University of Utah. The SDSS website is www.sdss.org.

DATA AVAILABILITY

The data underlying this article are available in the article and in its online supplementary material.

REFERENCES

- Ahumada R., et al., 2020, *ApJS*, 249, 3
 Assef R. J., et al., 2011, *ApJ*, 742, 93
 Bentz M. C., et al., 2006, *ApJ*, 651, 775
 Bon N., Bon E., Marziani P., Jovanović P., 2015, *Ap&SS*, 360, 7
 Collin S., Kawaguchi T., Peterson B. M., Vestergaard M., 2006, *A&A*, 456, 75
 Corbin M. R., 1995, *ApJ*, 447, 496
 Dalla Bontà E., et al., 2020, *ApJ*, 903, 112

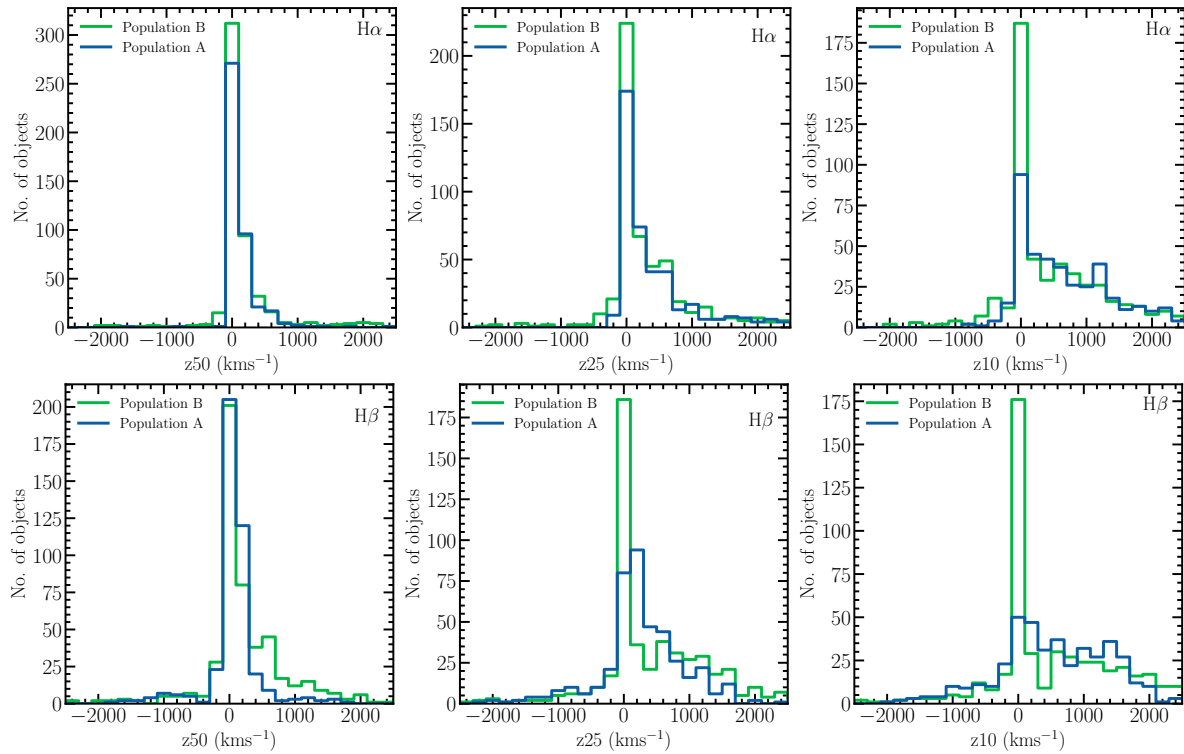


Figure 13. Histogram of the asymmetries measured at 50% (left panels), 25% (middle panels), and 10% (right panels) of line intensity for the broad $H\alpha$ (upper panels) and $H\beta$ line (bottom panels), for Population A (blue line) and Population B (green line) objects.

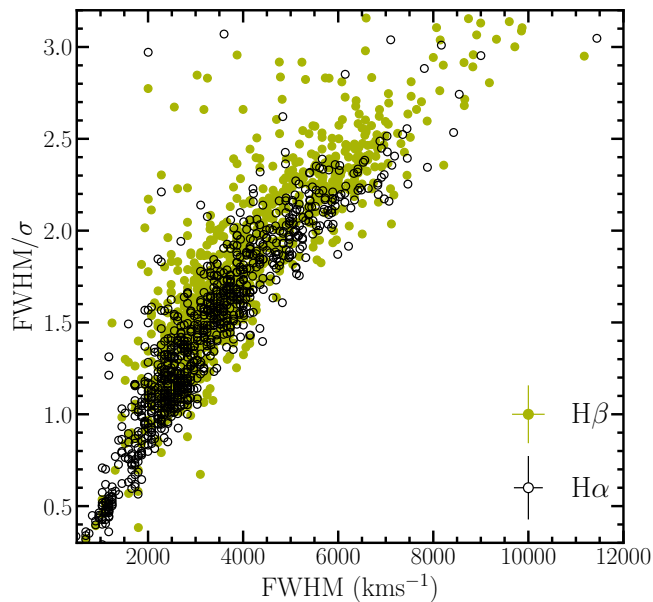


Figure 14. FWHM/σ vs. FWHM for $H\alpha$ line (open circles) and for $H\beta$ line (green circles). Mean error-bars are indicated on the plot.

Dimitrijević M. S., Popović L. Č., Kovačević J., Dačić M., Ilić D., 2007, *MNRAS*, **374**, 1181
 Dojčinović I., Kovačević-Dojčinović J., Popović L. Č., 2022, arXiv e-prints, p. arXiv:2204.10036
 Gaskell C. M., 2009, *New Astron. Rev.*, **53**, 140
 Greene J. E., Ho L. C., 2005, *ApJ*, **630**, 122
 Ilić D., et al., 2017, *Frontiers in Astronomy and Space Sciences*, **4**, 12

Ilić D., et al., 2020, *A&A*, **638**, A13
 Jonić S., Kovačević-Dojčinović J., Ilić D., Popović L. Č., 2016, *Ap&SS*, **361**, 101
 Kaspi S., Smith P. S., Netzer H., Maoz D., Jannuzi B. T., Giveon U., 2000, *ApJ*, **533**, 631
 Kollatschny W., 2003, *A&A*, **412**, L61
 Kollatschny W., Zetzl M., 2011, *Nature*, **470**, 366
 Kollatschny W., Zetzl M., 2013, *A&A*, **558**, A26
 Kormendy J., Ho L. C., 2013, *ARA&A*, **51**, 511
 Kovacevic A., Zekovic V., Ilic D., Arbutina B., Novakovic B., Onic D., Marceta D., Djosovic V., 2022, Publications of the Astronomical Society “Rudjer Boskovic”, **22**, 231
 Kovačević-Dojčinović J., Popović L. Č., 2015, *ApJS*, **221**, 35
 Kovačević-Dojčinović J., Dojčinović I., Lakićević M., Popović L. Č., 2022, *A&A*, **659**, A130
 Kovačević J., Popović L. Č., Dimitrijević M. S., 2010, *ApJS*, **189**, 15
 Liu H. T., Feng H. C., Bai J. M., 2017, *MNRAS*, **466**, 3323
 Liu H.-Y., Liu W.-J., Dong X.-B., Zhou H., Wang T., Lu H., Yuan W., 2019, *ApJS*, **243**, 21
 Liu H. T., Feng H.-C., Li S.-S., Bai J. M., 2022, *ApJ*, **928**, 60
 Marziani P., Sulentic J. W., 2012, *New Astron. Rev.*, **56**, 49
 Marziani P., Sulentic J. W., Zwitter T., Dultzin-Hacyan D., Calvani M., 2001, *ApJ*, **558**, 553
 Marziani P., et al., 2018, in Revisiting Narrow-Line Seyfert 1 Galaxies and their Place in the Universe. p. 2 (arXiv:1807.03003)
 Marziani P., et al., 2022a, arXiv e-prints, p. arXiv:2205.07034
 Marziani P., et al., 2022b, *Astronomische Nachrichten*, **343**, e210082
 McLure R. J., Dunlop J. S., 2001, *MNRAS*, **327**, 199
 McLure R. J., Jarvis M. J., 2002, *MNRAS*, **337**, 109
 Mediavilla E., Jiménez-Vicente J., Fian C., Muñoz J. A., Falco E., Motta V., Guerras E., 2018, *ApJ*, **862**, 104
 Mejía-Restrepo J. E., Trakhtenbrot B., Lira P., Netzer H., Capellupo D. M., 2016, *MNRAS*, **460**, 187
 Netzer H., 1977, *MNRAS*, **181**, 89
 Netzer H., 2013, The Physics and Evolution of Active Galactic Nuclei

- Netzer H., 2015, [ARA&A](#), **53**, 365
- Osterbrock D. E., Ferland G. J., 2006, *Astrophysics of gaseous nebulae and active galactic nuclei*
- Peterson B. M., 2014, [Space Sci. Rev.](#), **183**, 253
- Peterson B. M., Wandel A., 1999, [ApJ](#), **521**, L95
- Peterson B. M., et al., 2004, [ApJ](#), **613**, 682
- Popović L. Č., 2020, [Open Astronomy](#), **29**, 1
- Popović L. Č., Mediavilla E., Bon E., Ilić D., 2004, [A&A](#), **423**, 909
- Popović L. Č., Kovačević-Dojčinović J., Marčeta-Mandić S., 2019, [MNRAS](#), **484**, 3180
- Punsly B., Marziani P., Berton M., Kharb P., 2020, [ApJ](#), **903**, 44
- Schlegel D. J., Finkbeiner D. P., Davis M., 1998, [ApJ](#), **500**, 525
- Shapovalova A. I., et al., 2012, [ApJS](#), **202**, 10
- Shen Y., Ho L. C., 2014, [Nature](#), **513**, 210
- Shen Y., et al., 2011, [ApJS](#), **194**, 45
- Smee S. A., et al., 2013, [AJ](#), **146**, 32
- Sulentic J. W., Marziani P., Dultzin-Hacyan D., 2000, [ARA&A](#), **38**, 521
- Sulentic J. W., Marziani P., Zamanov R., Bachev R., Calvani M., Dultzin-Hacyan D., 2002, [ApJ](#), **566**, L71
- Vanden Berk D. E., et al., 2006, [AJ](#), **131**, 84
- Vestergaard M., Peterson B. M., 2006, [ApJ](#), **641**, 689
- Vietri G., et al., 2020, [A&A](#), **644**, A175
- Xiao T., Barth A. J., Greene J. E., Ho L. C., Bentz M. C., Ludwig R. R., Jiang Y., 2011, [ApJ](#), **739**, 28
- Yip C. W., et al., 2004a, [AJ](#), **128**, 585
- Yip C. W., et al., 2004b, [AJ](#), **128**, 2603
- Zamfir S., Sulentic J. W., Marziani P., Dultzin D., 2010, [MNRAS](#), **403**, 1759
- Zheng W., Sulentic J. W., 1990, [ApJ](#), **350**, 512

This paper has been typeset from a $\text{\TeX}/\text{\LaTeX}$ file prepared by the author.